International Journal of Thermal Sciences 145 (2019) 106033

Contents lists available at ScienceDirect

International Journal of Thermal Sciences

journal homepage: www.elsevier.com/locate/ijts

The connection between wall wettability, boiling regime and symmetry breaking for nanoscale boiling

Longyan Zhang[a], Jinliang Xu[a,b,*], Junpeng Lei[a], Guanglin Liu[a]

[a] Key Laboratory of Condition Monitoring and Control for Power Plant Equipment of Ministry of Education, North China Electric Power University, Beijing, 102206, China
[b] Beijing Key Laboratory of Multiphase Flow and Heat Transfer, North China Electric Power University, Beijing, 102206, China

ARTICLE INFO

Keywords:
Nanoscale boiling
Boiling regime
Surface wettability
Leidenfrost
Symmetry breaking

ABSTRACT

The effect of surface wettabilities on nanoscale boiling is investigated using molecular dynamics simulation. Argon particles are filled in-between two solid walls to form a vapor-liquid system. Surface wettability and fluid densities are controlled by the solid-liquid interaction intensity and the number of argon particles, respectively. A complete boiling regime map is presented. At high fluid densities ($\rho > 0.8\rho_{sat}$, where ρ_{sat} is the saturation liquid density), non-boiling regime occurs independent on surface wettabilities. At low fluid densities ($\rho \leq 0.8\rho_{sat}$), Leidenfrost, heterogeneous and homogeneous regimes consecutively occur when surface wettabilities are changed from super-hydrophobicity to super-hydrophilicity. Leidenfrost regime is recognized as a nanoscale lotus-leaf-effect. Both Leidenfrost and homogeneous regimes generate symmetric fluid densities. For heterogeneous nucleation, bubble nucleation occurs on either one of the two walls. Because the symmetry of the stable state of the system is lower than the symmetry of the solid-fluid interaction potentials, a small disturbance may change the wall to nucleate a bubble embryo, resulting in asymmetric fluid densities to cause the symmetry breaking. The present study enhances the understanding of nanoscale boiling.

1. Introduction

Boiling widely takes place in thermal power generation systems and it is an efficient way to dissipate high heat fluxes for thermal management of electronic devices and fuel cells [1]. The study of boiling started from 18th century [2]. The classic bubble nucleation theory tells us that the change in availability during heterogeneous nucleation at equilibrium is [3].

$$\Delta\psi_c^{het} = \frac{\pi\gamma_{lv} r_c^2 (2 + 3\cos\theta - \cos^3\theta)}{3} \quad (1)$$

where γ_{lv} is the surface tension between liquid and vapor, r_c is the critical radius of a bubble embryo, and θ is the contact angle. When θ equals to 0°, Eq. (1) is simplified as

$$\Delta\psi_c^{hom} = \frac{4\pi\gamma_{lv} r_c^2}{3} \quad (2)$$

Eqs. (1) and (2) show that for superheated liquid at uniform temperature, homogeneous nucleation requires more work to achieve than heterogeneous nucleation, but the transition boundary between homogeneous and heterogeneous nucleation remains unknown. Molecular dynamic simulation (MD) is effective to study nanoscale boiling. Recent progress focused on the effect of surface wettabilities. Considering a thermal system having two walls separated by liquid, boiling depends on wall material, working fluid and temperatures. Surface wettability, characterized by contact angle, can be determined by the solid-liquid interaction intensity, i.e., the intermolecular force interaction between solid and liquid atoms. Table 1 lists some boiling studies dependent on surface wettabilities. There are two methods to deal with boiling. The first one involves two walls filled with a specific density fluid. Boiling can be initialed by varying system pressures or fluid densities [4–7]. The location of a bubble embryo satisfies the minimum Gibbs free energy principle [3]. The second method deals with the wall heating system [8–18].

Even though many articles have been published, boiling on varied wettabilities with micro/nano structures is not fully understood. Usually, boiling is investigated in a narrow data range. A limited contact angles are considered, in which Yamamoto et al. [8] used three θ of 18°, 52° and 127°, Chen et al. [9] used four θ of 0°, 95°, 150° and 180°, and Novak et al. [11,12] used two θ of 22° and 129°. Due to the limited contact angles used, a complete boiling regime map is not available. In addition, current studies achieve contradictory conclusion regarding

* Corresponding author. Key Laboratory of Condition Monitoring and Control for Power Plant Equipment of Ministry of Education, North China Electric Power University, Beijing, 102206, China.
E-mail address: xjl@ncepu.edu.cn (J. Xu).

https://doi.org/10.1016/j.ijthermalsci.2019.106033
Received 12 February 2019; Received in revised form 17 July 2019; Accepted 19 July 2019

Table 1
The related boiling study dependent on wall wettabilities in the literature.

References	Surface	Fluid	Research methods	Findings and comments
Wei et al. [4]	Two LJ potential walls having θ = 142°-158°	LJ fluid	MD with nano-bubble formation by varying system pressures	Nano-bubble occurs in hydrophobic dot with varied bubble interface curvature during growing.
She et al. [5].	Platinum surface having six θ from 0° to 180°	Argon atoms	MD with constant system temperature but changing initial liquid densities	Homogeneous nucleation for hydrophilic wettability but heterogeneous nucleation in hydrophobic cavity.
Weijs et al. [6]	General LJ potential walls	LJ liquid with dissolved gas	MD with varied gas concentration in liquid	For a strong gas-solid attraction, the surface nano-bubble is sitting on a gas layer.
Nagayama et al. [7]	Platinum walls having six θ from 0° to 180°	Argon atoms	MD with constant system temperature but changing initial liquid densities	Homogeneous nucleation for hydrophilic wall but heterogeneous nucleation for hydrophobic wall. Internal pressure of nano-bubble does not agree with the Young-Laplace equation.
Yamamoto et al. [8]	A single LJ potential wall having three θ = 18°, 52° and 127°	General LJ potential liquid	MD with heating via the wall	Nano-bubble occurs in liquid which is several nanometers away from the wall. Hydrophilic wall promotes bubble formation.
Chen et al. [9]	A single platinum wall having four θ = 0°, 95°, 150° and 180°	Argon atoms	MD with heating via the wall	Bubble embryo prefers to occur in hydrophobic cavity.
Wang et al. [10]	A single copper wall with hydrophilic wettability	Subcooled water	MD with heating via the wall	Nano-bubbles are observed by increasing wall superheating. They are merged to form a vapor layer on the wall surface.
Novak et al. [11,12]	A single LJ potential wall having two θ = 22° and 129°	Argon atoms	MD with constant system pressure and heating via the wall	Nucleation rate on hydrophobic wall is higher than on hydrophilic wall.
Carey et al. [13]	A single gold wall with hydrophilic wettability	Argon atoms	MD with heating via the wall together with the thermodynamic analysis	The wall attraction to liquid results in homogeneous nucleation, taking place at a location slightly away from solid surface.
Hens et al. [14]	A single platinum wall having three θ = 43°, 96° and 132°	Argon atoms	MD with heating via the wall	Hydrophilic surfaces provide favorable conditions for bubble nucleation and formation of vapor films.
Wang et al. [15]	A single platinum wall having two θ = 43° and 132°	Argon atoms	MD with heating via the wall	Explosive boiling prefers to occur having hydrophilic wettability and there is an adsorption layer composed of several layers of liquid argon atoms on hydrophilic wall.
Fu et al. [16]	A single copper wall with hydrophilic wettability	Water	MD with heating via the wall	The temperature of the water film when it separates from solid surface increase with increasing size of nanostructure.
Shavik et al. [17]	A platinum wall with hydrophilic and hydrophobic wettability	Argon atoms	MD with heating via the wall	The hydrophilic surface provides more favorable conditions for boiling than the hydrophobic surface
Wang et al. [18]	A single aluminum wall having one θ = 120°	Argon atoms	MD with heating via the wall	The nanostructures raise the heat transfer efficiency and evaporation rate increases with the nanostructures height in a certain range.
Schoen et al. [19]	Platinum walls having θ = 119°	Argon atoms	MD with constant system volume and cooling via the wall	The crystallization of liquid atoms starts from bottom wall to generate a “frozen” bubble on top wall.
Gong et al. [20,21]	General solid walls having two θ = 53° and 103°	Water	Lattice Bolzman simulation	Bubble nucleation begins in a hydrophilic cavity center, but it starts from a hydrophobic cavity corner. The nucleation time in a hydrophobic cavity is much shorter than that in a hydrophilic cavity.
Jo et al. [22]	A single silicon substrate with two θ = 54° and 123°	Water	Experimental study with pooling boiling	Heterogeneous boiling occurs on both of hydrophilic and hydrophobic surfaces. Hydrophobic surfaces offer better boiling heat transfer than hydrophilic surfaces at very low heat fluxes.
Lee and Song [23]	A single silicon substrate with three θ = 67°, 100° and 126°	Water drop	Experimental study with heating via the wall	The Leidenfrost layer beneath a water drop occurs on both hydrophobic surface and nanotextured Cassie surface to result in a slow drop evaporation.
Dupeux et al. [24]	The superhydrophobic brass substrate machined to achieve ratchets	Water drop with the radius of 2.9–5 mm	Experimental study with heating via the wall.	The super-hydrophobic ratchet realizes the quick self-propulsion of a droplet with a lower substrate temperature, implying that levitation is not necessary to induce the motion.
Malavasi et al. [25]	Stainless steel substrates having advancing θ = 29° −153°	Water	Experimental study with heating via the wall.	Bubbles are easier to form on superhydrophobic surfaces, which present a “quasi-Leidenfrost” regime for low superheat.
Hsu et al. [26]	General solid wall with θ = 5° −180°	Water	Numerical simulation with volume of fluid (VOF) method.	The Leidenfrost temperature decreases with increasing contact angle.

the wettability effect. Most of authors noted homogeneous nucleation in hydrophilic system, and heterogeneous nucleation in hydrophobic system [7–13]. However, Hens et al. [14] showed that a bubble does not form easily on a non-wetting surface. Hydrophilic surfaces provide favorable conditions for bubble nucleation and formation of vapor films. Wang et al. [15] indicated that explosive boiling prefers to occur with a hydrophilic wall and there is an additional liquid layer separating vapor and wall. The reason for the above contradiction remain unknown yet.

Leidenfrost vapor is another phase pattern, which was first documented by Leidenfrost around 1750 [27]. For a droplet on a wall, if the wall has much higher temperature than the saturation temperature of liquid, the droplet does not boil but evaporates with a slow evaporation rate. A vapor layer on the wall separates wall from liquid, deteriorating heat mass transfer. The Leidenfrost effect has been paid great attention in recent years. The available studies focused on the heat transfer induced Leidenfrost vapor on the wall [22,23]. For a vapor-liquid system, it is possible to re-organize the two-phase structure by changing surface wettabilities, which is one of our interests in this paper.

In this paper, boiling is comprehensively investigated considering the effects of surface wettability and liquid saturation degrees. A complete boiling regime map is constructed, including non-bubble-nucleation regime, homogeneous nucleation, heterogeneous nucleation, and Leidenfrost regime. For heterogeneous nucleation, the symmetry breaking resulted from random nano-bubble formation in either one of the two walls is discussed. For super-hydrophobicity system, the Leidenfrost phenomenon was observed in nanoscale. This phenomenon is caused by ultra-low surface energy, which is different from that resulted from ultra-high wall temperature reported in literature [22,23].

2. The MD simulation of the studied problem

The studied problem includes two platinum walls and argon liquid in-between (see Fig. 1a). The computation domain has $L_x = 17.15\sigma$, $L_y = 11.3\sigma$ and $L_z = 21.2\sigma$, where σ is the length scale of argon atom. Periodic boundary conditions are applied along x and y directions. The thickness of liquid film is $H = 16\sigma$. The two solid walls are kept as 100 K, and the non-dimensional temperature is $T^* = 0.827$. The saturation liquid density ρ_{sat} is 1310 kg/m^3 at a temperature of 100 K, under which the non-dimensional saturation liquid density is $\rho^*_{sat} = 0.7818$. Covering the whole data range, fluid densities vary from $0.6\rho_{sat}$ to $0.9\rho_{sat}$, where the coefficient 0.6–0.9 is called the saturation degree. Correspondingly, there are 1496 and 2340 argon atoms at the saturation degree of 0.6 and 0.9, respectively. A higher saturation degree corresponds to smaller vapor void in the two-phase system at equilibrium state.

Careful attention was paid to the size of the MD simulation box. In the present study, the three lengths are set as 17.15σ, 11.3σ and 21.2σ in the three coordinates of x, y and z. Generally, the length in each coordinate should be larger than the cut-off distance, which is $\sim 3\sigma$ for MD simulation. We note that periodic boundary conditions were used along x and y coordinates. The lengths of 17.15σ in x direction and 11.3σ in y direction are sufficient to produce accurate and reasonable results. The length in z direction is important to capture the key microscopic phenomenon. Again, the length in z direction should also be larger than the cut-off distance of 3σ. In this paper, the most important concern is to deal with the solid-fluid interaction in z direction. Too large length in z direction (for example, $L_z > 100\sigma$) may weaken the effect of the intermolecular solid-fluid interaction on the phase pattern transition. In summary, $L_x = 17.15\sigma$, $L_y = 11.3\sigma$ and $L_z = 21.2\sigma$ not only ensure accurate simulation results, but also capture important phenomenon in nanoscale. Such size was also used in Ref. [7].

All solid atoms are assumed in face-centered-cubic (fcc) structure at the start of computation. Each wall has eight layers, including 2688 atoms corresponding to a density of 21.45×10^3 kg/m^3. Based on the wall model of Yi et al. [28], among the eight layers, the four layers

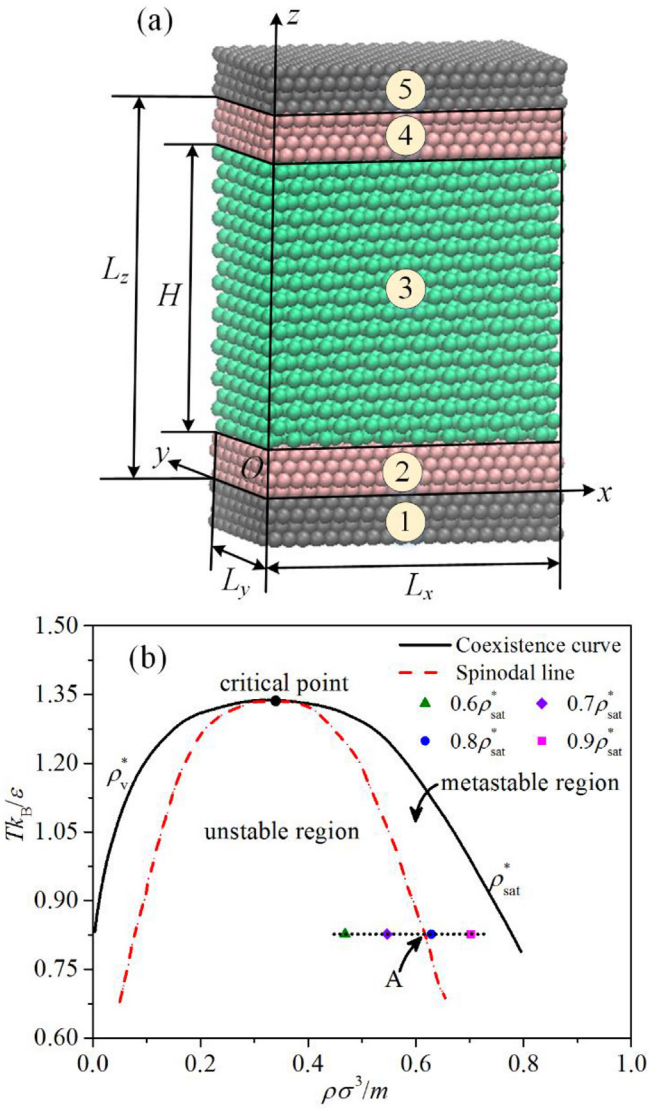

Fig. 1. The studied problem (a: 1 and 5 are ghost atoms, 2 and 4 are wall atoms, 3 is liquid atoms; b: simulation points and phase diagram with coexistence curve and spinodal line with $\rho^*_{sat} = 0.7818$ and $T^* = 0.827$).

Table 2
The non-dimensional parameters.

Property	Parameters
Length	$r^* = \frac{r}{\sigma}$
Time	$t^* = \frac{t}{\tau}$
Force	$F^* = \frac{F\sigma}{\varepsilon}$
Temperature	$T^* = \frac{k_B T}{\varepsilon}$
Velocity	$v^* = \frac{v\tau}{\sigma}$
Density	$\rho^* = \frac{\rho\sigma^3}{m}$

contacting the liquid are oscillating freely, the next two layers act as the thermostat to keep constant wall temperature, and the outmost two layers are stationary to “frozen” the solid wall. The thermostat atoms and stationary atoms are called ghost atoms. The following equation is used to satisfy the thermostat principle [28].

$$\frac{dp_i}{dt} = -\xi p_i + F(t) + f(t) \tag{3}$$

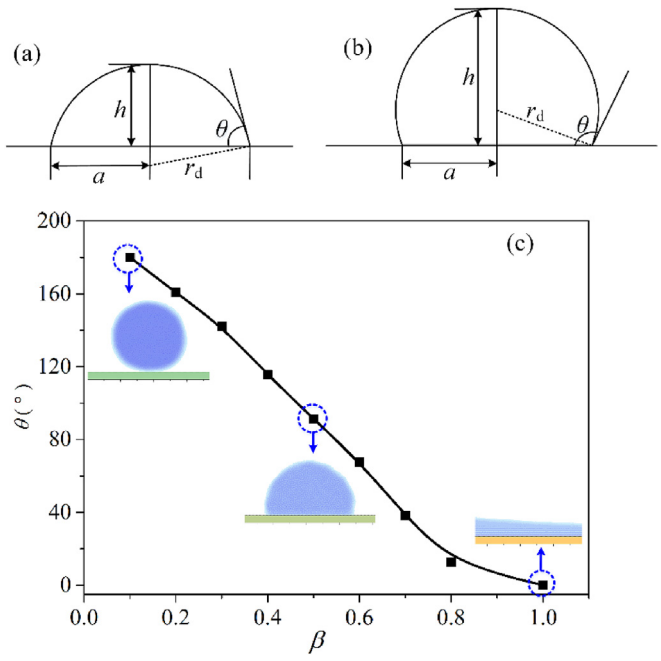

Fig. 2. Effect of β on contact angles on the wall ($\alpha = 0.14$).

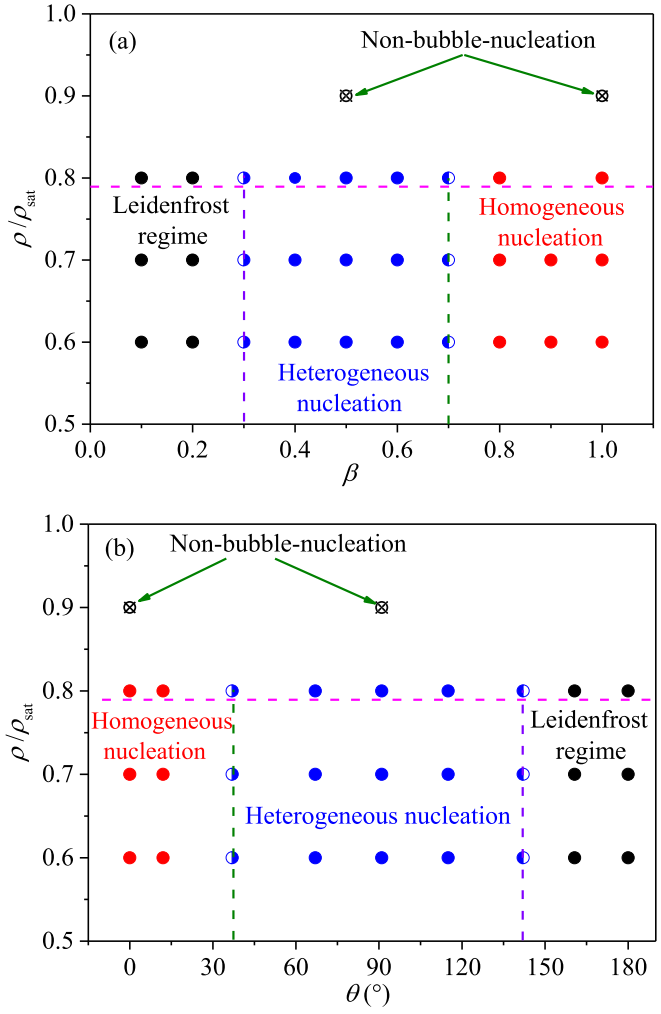

Fig. 3. The boiling regime map dependent on surface wettabilities and initial liquid densities.

where p_i is the momentum vector of ith solid atom, $\xi = 168.3\tau^{-1}$ is the damping constant, $F(t)$ is the interaction force between atoms, $f(t)$ is the exciting force vector, which is randomly sampled from Gaussian distribution with zero mean average value and standard deviation of $\sigma_G = \sqrt{2\xi k_B T/\Delta t}$, $k_B = 1.38 \times 10^{-23}$ J/K is the Boltzmann constant and $\Delta t = 0.001\tau$ is the time step, $\tau = \sqrt{m\sigma^2/\varepsilon}$ is the time scale, m is the atom mass. The thermostat atoms not only keep the constant wall temperature, but also are oscillating to exchange the energy with the inner four layers. Thus, the thermostat atoms cannot be fixed. The outmost stationary layers are helpful to ensure the numerical convergence during simulation. In microscale, temperature represents the kinetic energy of atoms. It is not necessary to assign a temperature for the fixed atoms.

The Newton equation is written for each atom as

$$m\frac{d\vec{r}^2}{dt^2} = \sum_{j\neq i,j=1}^{N} \vec{F}_{ij} + \sum_{j_s\neq i,j=1}^{N_s} \vec{F}_{ij_s} \tag{4}$$

where F_{ij} refers to the pair interaction force between liquid atoms, and F_{ij_s} represents the pair interaction force between liquid and solid atoms, r is the distance between two atoms, N and N_s are the number of liquid atoms and solid atoms, respectively. The pair interaction force is written as

$$F_{ij} = -\frac{\partial \varphi_{ij}}{\partial r_{ij}} \tag{5}$$

The Lennard-Jones (L-J) potential is

$$\varphi_{LJ}(r) = 4\alpha\varepsilon_{LJ}\left[\left(\frac{\sigma_{LJ}}{r}\right)^{12} - \beta\left(\frac{\sigma_{LJ}}{r}\right)^{6}\right] \tag{6}$$

where ε_{LJ} is the energy scale and σ_{LJ} is the length scale. Potential energy factors α and β are used to adjust the strength of hydrophilic interaction and hydrophobic interaction. Equation (6) uses α and β to characterize the surface wettability [7]. The surface wettability is more sensitive to the variations of α than to the variations of β. A small change of α results in a large variation of contact angle. Thus, we keep α as a constant. Our numerical test shows that $\alpha = 0.14$ is an "optimal" value to ensure a gradual transition from super-hydrophilicity to super-hydrophobicity when β is continuously changed. Other α values deviating from 0.14 is not necessary to be used. Similar treatment can be seen in Ref. [7]. For solid-solid and liquid-liquid computations, the parameters are set as $\alpha = 1$ and $\beta = 1$. The parameters are $\varepsilon = 1.67 \times 10^{-21}$ J and $\sigma = 3.405 \times 10^{-10}$ m for argon atoms, and they are $\varepsilon_s = 8.35 \times 10^{-20}$ J and $\sigma_s = 2.475 \times 10^{-10}$ m for solid atoms. For solid-liquid interaction, $\varepsilon_{ls} = \sqrt{\varepsilon \cdot \varepsilon_s}$ and $\sigma_{ls} = 0.5(\sigma + \sigma_s)$ are applied, which is called the Lorentz-Berthelot combining rule [29]. Because the liquid-liquid interaction uses specific energy scale and length scale, the fluid is argon. The solid-liquid interaction uses varied β to simulate the varied surface wettabilities. Solid can be considered to have general atoms. The objective of this paper is to study the effect of surface wettability on nanoscale boiling, the surface with nano-structure is beyond the scope of this paper. Here, the nanoscale boiling refers to the channel height in nanoscale. The truncation radius of potential functions is set as 3σ, which is obviously smaller than the thickness of the solid atom layers of 5.2σ.

The Velocity-Verlet method is used to integrate the momentum equation and the cell subdivision technique is applied to improve the computational efficiency. The timestep is set as 0.001τ. The approaching-equilibrium-state stage and the data sampling stage are involved in our simulation. The former stage starts from the initial state to the end of 1000τ. After achieving an equilibrium state, the temperature is kept at $T = 0.827\varepsilon/k_B = 100$ K. Then, the data sampling is performed for a following 100τ. The simulation is conducted using the open-source Large-scale Atomic/Molecular Massively Parallel Simulator (LAMMPS) [30]. The VMD software is used for the atomic visualization.

Fluid density (ρ) and temperature (T) are averaged in each bin.

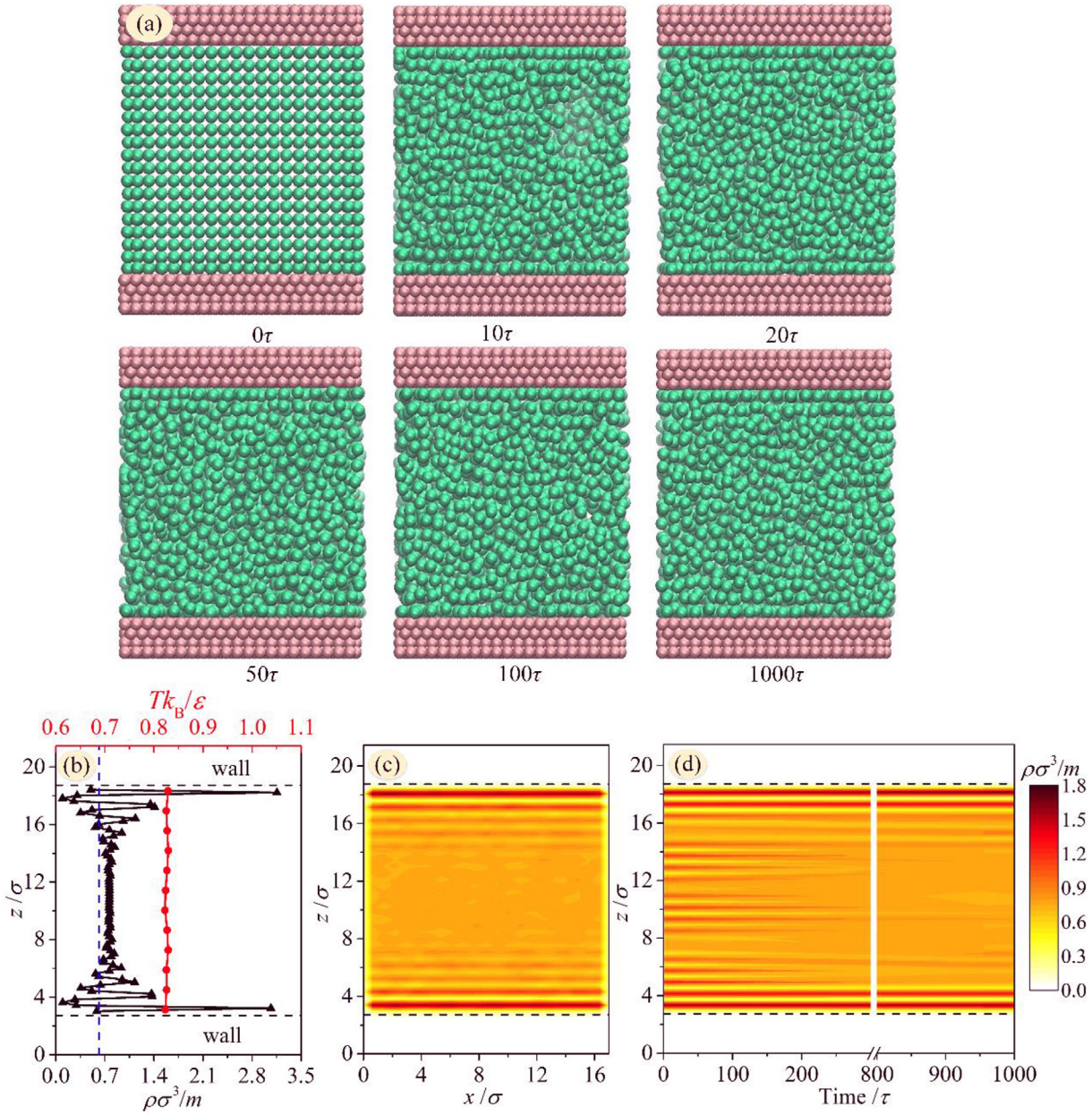

Fig. 4. Non-bubble-nucleation with $\theta = 0^o$, $\alpha = 0.14$, $\beta = 1.0$ and $\rho/\rho_{sat} = 0.9$ (a: non-bubble-nucleation, b: density and temperature distributions in channel height direction, c: liquid atoms distribution over the *xz* plane, d: density evolution versus time).

Totally 12 bins are segmented in liquid height direction for temperature computation. Temperature in the *i*th bin, T_i, is determined by the laboratory velocity v_j relative to the mean velocity u_i in three coordinates of *x*, *y* and *z*:

$$T_i = \frac{\sum_{j=1}^{N_i} m[(v_{j,x} - u_{i,x})^2 + (v_{j,y} - u_{i,y})^2 + (v_{j,z} - u_{i,z})^2]}{(3N_i - \delta)k_B} \quad (7)$$

where N_i is the number of argon atoms in *i*th bin, and δ is the number of degrees of freedom ($\delta = 3$).

In order to present results in a general sense, computations are performed using a set of non-dimensional parameters, which are expressed in Table 2. All the parameters are scaled by *m*, σ and ε of liquid atoms. Fig. 1b shows the density-temperature ($\rho - T$) curve for argon [31]. The coexistence curve represents the relationship between fluid density and temperature at equilibrium vapor-liquid state. The maximum point of the curve is the critical point. Interfaced at the critical point, the left part and right part represent saturation vapor densities ρ_v and saturation liquid densities ρ_{sat}, respectively. At saturation liquid state, the distance between liquid molecules cannot be further decreased to have a maximum ρ_{sat}. For any vapor-liquid system, fluid density should be larger than ρ_v and smaller than ρ_{sat}. The fluid density is written as $c\rho_{sat}$, where *c* is called the saturation degree which is smaller than 1. The coexistence curve corresponds to the $P - v$ and $P - T$ diagrams at equilibrium state, where *v* and *P* are specific volume and pressure, respectively. Vapor voids may not occur if fluid density only has a small deviation from ρ_{sat}. A spinodal curve exists [32,33]. The metastable region is located between the spinodal line and the coexistence curve. The high saturation fluid of $0.9\rho_{sat}$ is located in the metastable region. A low saturation fluid of $0.6–0.7\rho_{sat}$ is inside the metastable region envelope, behaving unstable feature to trigger the vapor voids easily. In our computations, pressure is considered. When the equilibrium state is reached, the pressure matches the saturation pressure corresponding to the temperature.

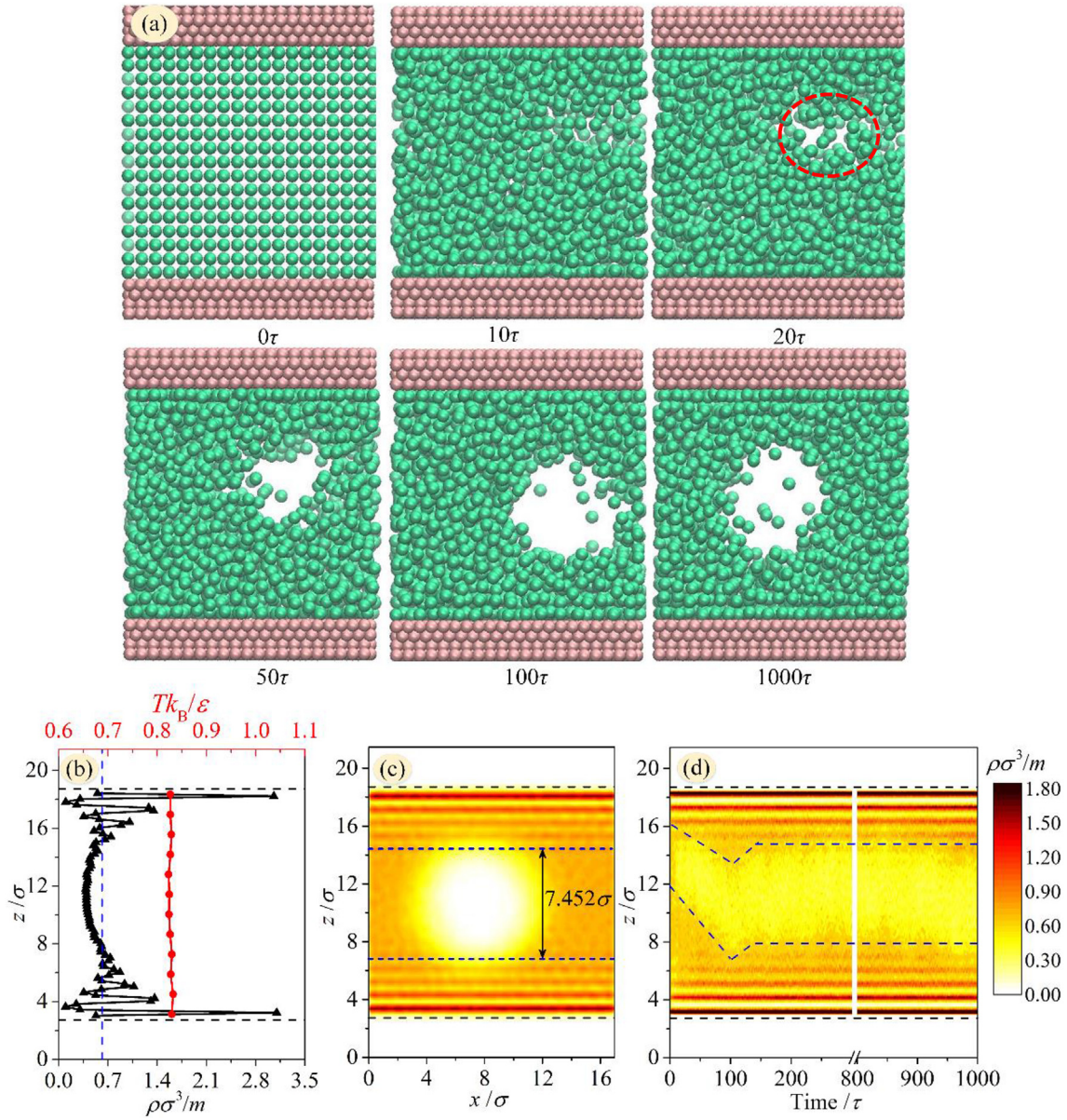

Fig. 5. Homogeneous bubble nucleation with $\theta = 0^{o}$, $\alpha = 0.14$, $\beta = 1.0$ and $\rho/\rho_{sat} = 0.7$ (a: bubble nucleation and growth in liquid volume, b: density and temperature distributions in channel height direction, c: steady bubble over the *xz* plane, d: density evolution versus time).

3. Contact angle dependent on α and β

In order to connect the contact angle θ and the interaction parameters of α and β, a separate MD simulation was performed. The whole computation domain sets $110\sigma \times 10\sigma \times 64\sigma$, containing 6690 argon atoms and 11566 solid atoms. The periodic boundary condition is applied along the axial direction *x* and the direction perpendicular to the paper plane *y*, yielding a two-dimensional droplet on a wall. At the initial condition of $t = 0$, zero liquid momentums along *x* and *y* directions are used to confine a droplet in the computation domain. Such constraint is only performed at $t = 0$. Following the start of the MD simulation ($t > 0$), each liquid atom receives forces from other liquid atoms and solid atoms in all the three directions of *x*, *y* and *z*, ensuring success drop spreading over the *xy* plane. Indeed, for contact angle calculation, the simulation box size is larger than that described in section 2. Especially, the sizes in *x* and *z* directions reach $\sim 100\sigma$, ensuring a smaller project area of droplet on the *xy* plane to determine the contact angle. Too small simulation box may cause the liquid film on the plane, introducing the difficulty to determine the contact angles.

The MD simulation keeps a typical NVT ensemble, i.e., constant number of particles, constant volume and constant temperature. Attention was paid on the solid layer structure to properly treat the solid-fluid interaction. Even though the simulation box is larger than that described in section 2, the solid layer structure in the height direction *z* is identical to that described in section 2. All solid atoms are assumed in face-centered-cubic (fcc) structure at the start of computation. Each wall has eight layers. Among the eight layers, the four layers contacting the liquid are oscillating freely, the next two layers act as the thermostat to keep constant wall temperature, and the outmost two layers are stationary to "frozen" the solid wall. The thermostat principle uses Eq. (3).

The equilibrium system temperature is set as $T = 0.827\varepsilon/k_B = 100$ K. The corresponding saturation pressure is 0.324 MPa. The argon density distribution is averaged over the *xz* plane with a grid resolution of $0.2\sigma \times 0.2\sigma$. The data sampling was repeated for each 100 timesteps. The location of 0.5 ($\rho_{sat} + \rho_v$) is defined as the vapor-liquid interface. Once the vapor-liquid interface does not change anymore, θ is computed based on droplet height *h* in *z* direction and

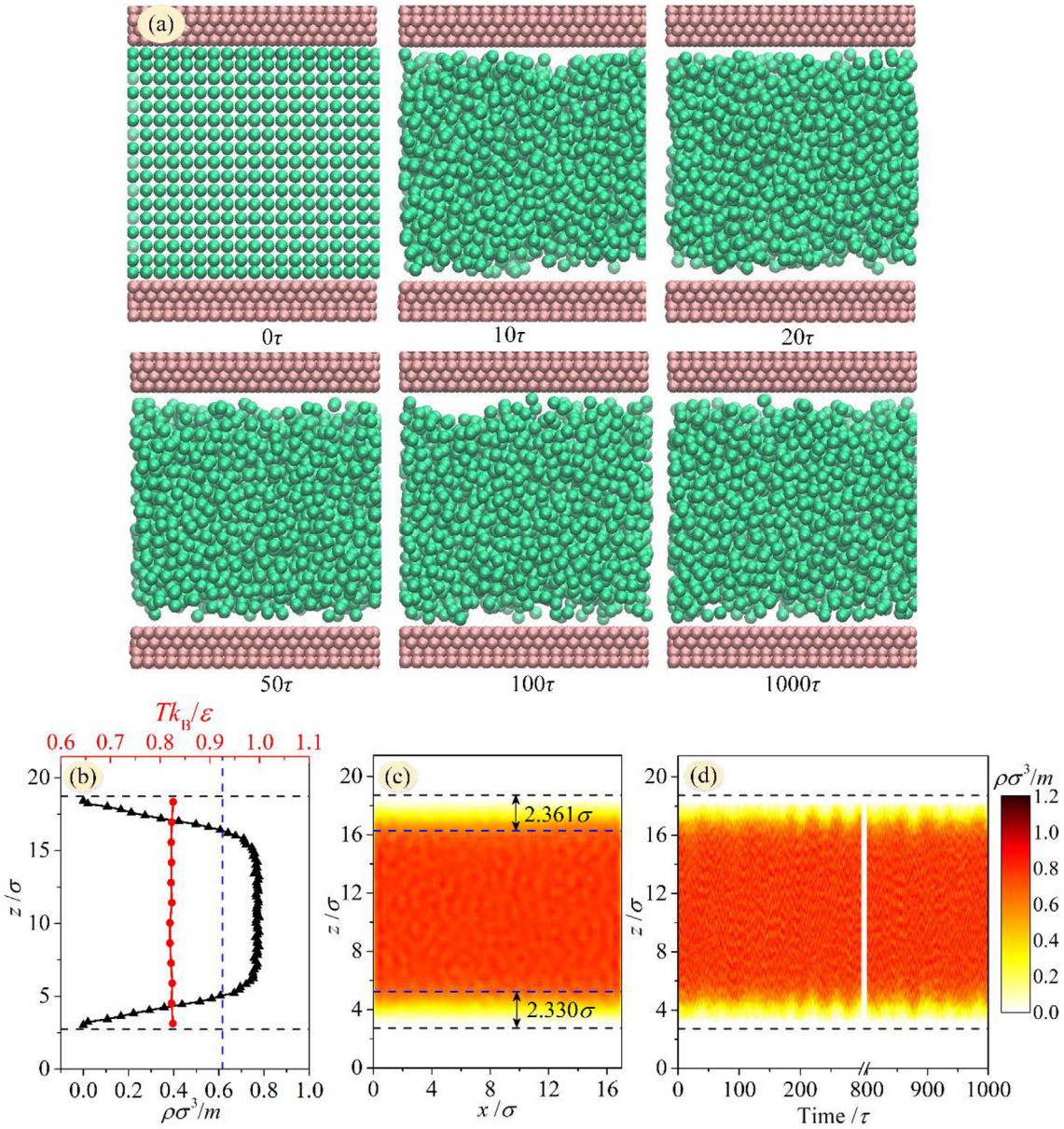

Fig. 6. The Leidenfrost layer formation with $\theta = 180^o$, $\alpha = 0.14$, $\beta = 0.1$ and $\rho/\rho_{sat} = 0.7$ (a: vapor layer formation on the wall, b: density and temperature distributions in channel height direction, c: steady vapor layer over the *x*z plane, d: density evolution versus time).

footprint radius a on the wall:

$$\theta = \begin{cases} \left|-\arcsin\left(\frac{a}{r_d}\right)\right| & \text{if } \theta < \frac{\pi}{2} \\ \pi - \arcsin\left(\frac{a}{r_d}\right) & \text{if } \theta > \frac{\pi}{2} \end{cases} \tag{8}$$

where $r_d = (a^2 + h^2)/(2h)$. Fig. 2 presents the simulation results, in which α is 0.14, but β is changed. Two limit cases are $\beta = 0.1$ corresponding to $\theta = 180^o$ (super-hydrophobic surface), and $\beta = 1.0$ corresponding to $\theta = 0^o$ (super-hydrophilic surface). Contact angles dependent on β are shown in Fig. 2c at the fixed $\alpha = 0.14$.

4. Results and discussion

The nanoscale boiling map is presented first. Different boiling regimes are then analyzed. Here, nanoscale refers to the thickness of liquid film confined in two walls, which is 16σ. At a specific fluid density, the minimum Gibbs free energy principle ensures the re-organization of fluid atoms to create different patterns. Fluid saturation degree and surface wettabilities dominate the transition boundaries between different regimes (see Fig. 3). Four regimes are identified to include a non-bubble-nucleation regime at $\rho > 0.8\rho_{sat}$ and three regimes of homogeneous, heterogeneous and Leidenfrost at $\rho \leq 0.8\rho_{sat}$. The latter three regimes consecutively occur with decrease of surface wettings from $\theta = 0^o$ to 180^o.

A wall is regarded as hydrophilic with $\theta < 90^o$, hydrophobic with $\theta > 90^o$ and super-hydrophobic with $\theta > 150^o$. Xie et al. [34] reported a critical contact angle of 147^o for the transition from hydrophobicity to super-hydrophobicity. This study supports the conclusion that "homogeneous nucleation prefers for wetting system, and heterogeneous nucleation prefers for non-wetting system" [5,7]. Attention is paid to the transition boundaries of contact angles. The heterogeneous regime corresponds to the range of $\theta = 37^o - 142^o$, showing that heterogeneous nucleation is still possible on hydrophilic wall, as long as $\theta > 37^o$. Besides, the super-hydrophobic wall does not trigger the heterogeneous nucleation, but triggers the Leidenfrost vapor on the

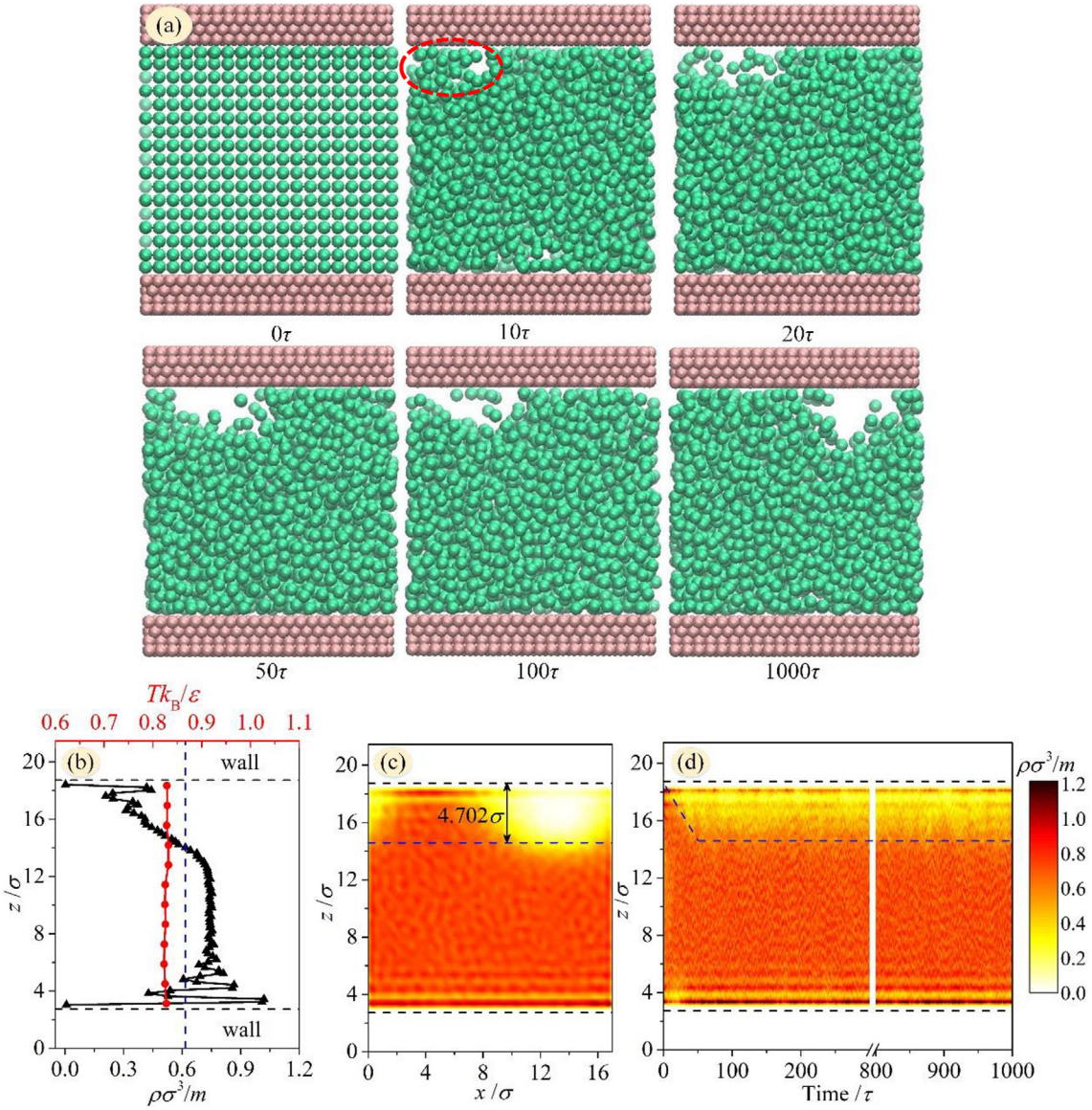

Fig. 7. Heterogeneous bubble nucleation with $\theta = 91.3^{\circ}$, $\alpha = 0.14$, $\beta = 0.5$, $\rho/\rho_{sat} = 0.7$ and $\Delta t = 0.001\tau$ (a: bubble nucleation and growth on the top wall, b: density and temperature distributions in channel height direction, c: steady bubble over the *xz* plane, d: density evolution versus time).

wall instead. Furthermore, the transition boundaries are influenced by fluid pressure/temperature, working fluid and system size. When these parameters are changed, the transition boundaries maybe different from those shown in Fig. 3, but the general trend should be identical.

4.1. The non-bubble-nucleation regime

For higher fluid density such as $\rho = 0.9\rho_{sat}$, fluid in metastable region is difficult to trigger the formation of a bubble embryo, yielding non-bubble-nucleation (see Fig. 4). Fluid temperature keeps uniform across the channel height, but densities are oscillating near the wall, beyond which fluid atoms are uniformly populated. Because liquid atoms are closely packed with each other, the distance between two liquid atoms is confined in a limited range. The liquid atoms either cannot be separated to become faraway, or cannot merge to become closer. The non-bubble-nucleation is further analyzed as follows. Assuming a growing nanobubble, because vapor density is 2–3 magnitudes smaller than liquid density, the liquid atoms initially in the bubble should be expelled outside of the bubble, resulting in closer arrangement of liquid atoms beyond the bubble interface. Due to the shortened distance of liquid atoms, the enlarged repulsive force pulls extra liquid atoms back to the bubble. The bubble embryo is shrinking due to the returning atoms. The non-bubble-nucleation regime is independent on surface wettabilities.

The vapor-liquid interface should be identified for nanoscale boiling. Because fluid densities are changed from liquid density to vapor density in a very narrow thickness across the interface, the interface identification is difficult. Here, vapor-liquid interface is assumed to have a density determined on the spinodal curve at the saturation temperature (see the crossing point A in Fig. 1b). If the local fluid density is smaller than the determined value, the local region is in vapor phase. Otherwise, the local region is in liquid phase. In Fig. 4b, the blue line represents the spinodal curve determined density to judge vapor-liquid interface. Because fluid densities in the bulk fluid region approach the spinodal curve determined density, vapor bubble is not detected in Fig. 4b.

4.2. Symmetry of homogeneous nucleation and Leidenfrost regimes

Once fluid is located in unstable region (see Fig. 1b), the surface

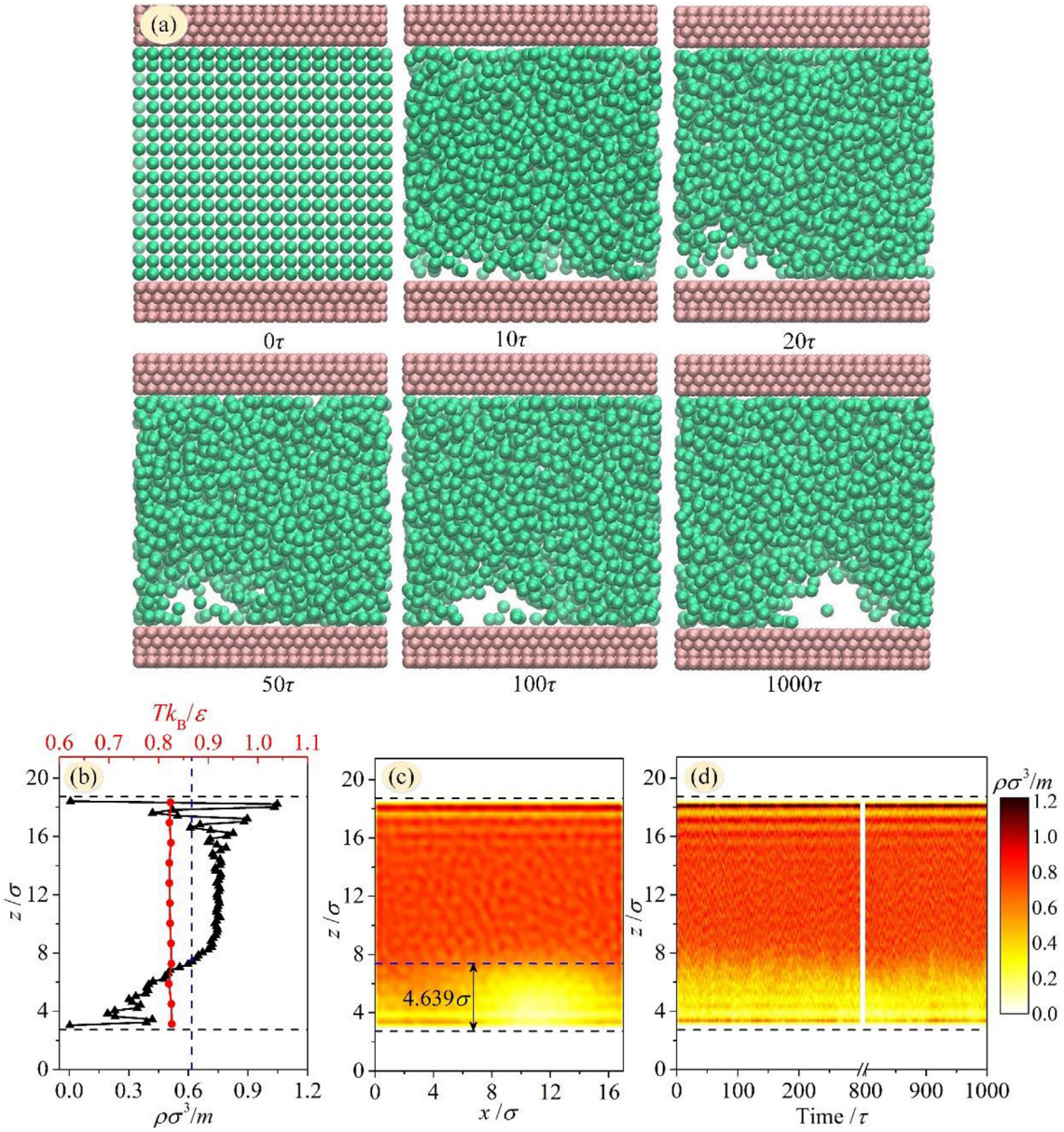

Fig. 8. Heterogeneous bubble nucleation with $\theta = 91.3^{o}$, $\alpha = 0.14$, $\beta = 0.5$, $\rho/\rho_{sat} = 0.7$ and $\Delta t = 0.0015\tau$ (a: bubble nucleation and growth on the bottom wall, b: density and temperature distributions in channel height direction, c: steady bubble over the *xz* plane, d: density evolution versus time).

wetting plays important role to determine boiling patterns. Because homogeneous nucleation and Leidenfrost regime create symmetry parameters, they are examined first. The heterogeneous nucleation results in symmetry breaking, which is analyzed in section 4.3.

Homogeneous nucleation takes place on super-hydrophilic walls ($\theta < 37^{o}$). The wall attraction is so strong that the near-wall-atoms are difficult to be separated. Super-hydrophilic wall with high energy surface confines liquid atoms near the wall. Initially the fluid density is low. The only way to minimize the Gibbs free energy is to re-assemble fluid atoms somewhere away from the wall, which is the basic mechanism for homogeneous nucleation. Following 0τ, a bubble embryo forms in bulk fluid instead on the wall, then grows and finally achieves a maximum size during 100-1000τ (see Fig. 5). The steady bubble diameter attains 7.452σ, whose volume is equivalent to that expels extra argon atoms from bubble to generate saturation liquid beyond the bubble interface.

Fluid densities, temperatures and bubble morphology are symmetrically populated against the system symmetry plane. Fluid densities are significantly large and oscillating near the wall, but they behave a parabola distribution in bulk fluid. The bubble location may deviate from the center along *x*-direction. This does not break the symmetry feature due to periodic boundary conditions in *x* and *y* coordinates. The center bubble location in channel height satisfies the symmetry rule. The homogeneous nucleation regime agrees with Refs. [5,7]. The difference between the present study and others is the transition contact angles from homogeneous nucleation to heterogeneous nucleation, which are seldomly reported [4–8].

In this paper, super-hydrophobic wall with $\theta > 142^{o}$ is an extreme wettability to induce Leidenfrost (see Fig. 6). Due to weak interaction between solid and fluid atoms, large repulsive force pushes fluid atoms from the wall to the bulk liquid, forming liquid phase in channel core. The blue line determined by the spinodal curve in Fig. 1b characterizes the vapor-liquid interface. Two vapor layers are formed on the two walls following $t > 10\tau$. Once the steady state is reached, the vapor layer thickness attains around 2.345σ. Because vapor and liquid phases reach thermal equilibrium, fluid temperature keeps uniform along the

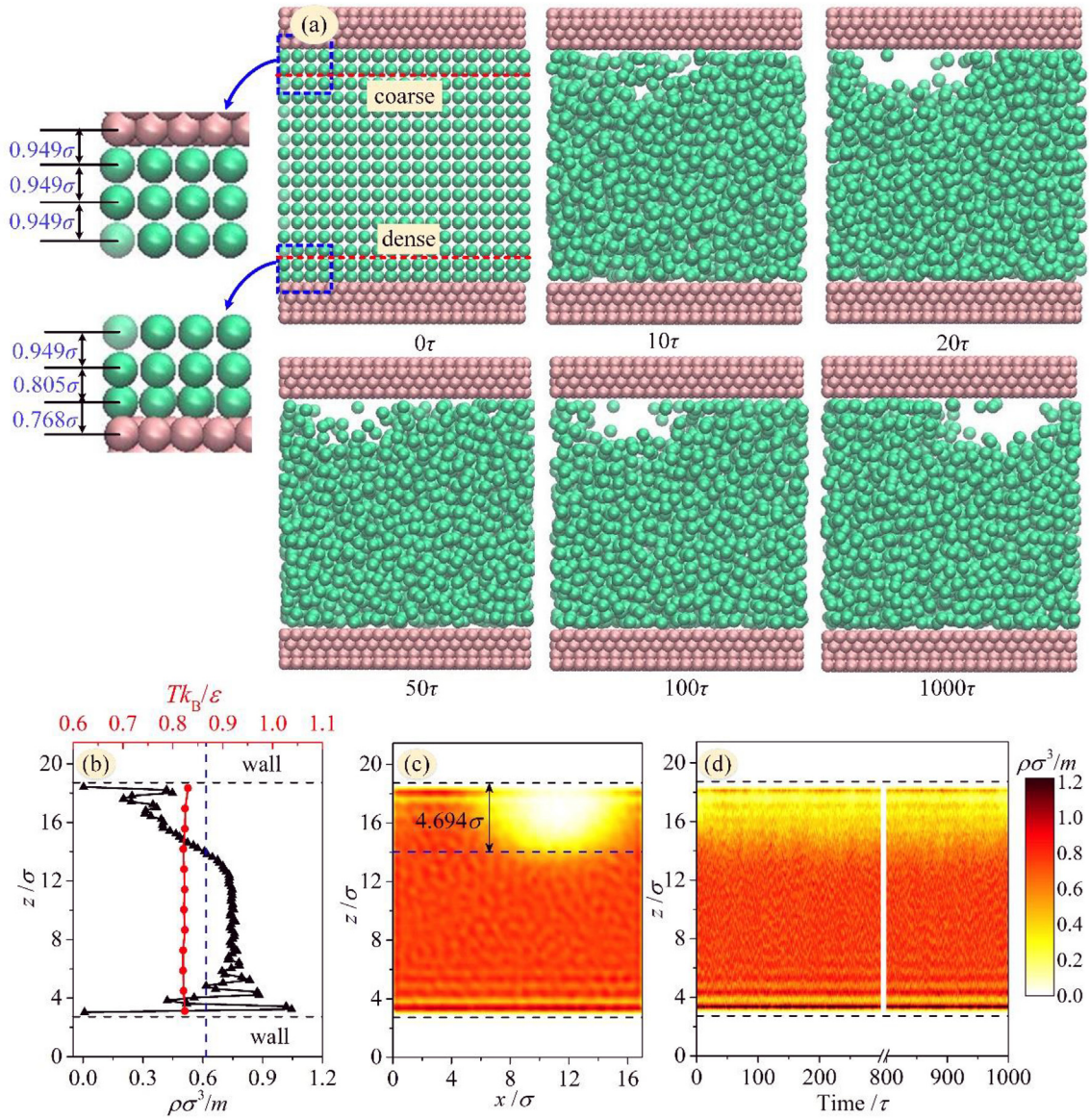

Fig. 9. Heterogeneous bubble nucleation with $\theta = 91.3^{o}$, $\alpha = 0.14$, $\beta = 0.5$, $\rho/\rho_{sat} = 0.7$ and denser liquid atoms population near bottom wall (a: bubble nucleation and growth on top wall, b: density and temperature distributions in channel height direction, c: steady bubble over the *xz* plane, d: density evolution versus time).

channel height. However, fluid densities are significantly low near the wall but have monotonic rise to achieve a flat distribution beyond the vapor-liquid interface, which are different from the homogeneous nucleation pattern.

Conventionally, the Leidenfrost layer is caused by sufficiently higher wall temperature than the saturation temperature of liquid. Here, the Leidenfrost layer is caused by the self-assembly of two-phase structure when super-hydrophobic walls are involved in the system. This finding is useful for the development of nano-device. Pressure drop is ultra-large for nanoflow. Based on the present finding, the super-hydrophobic nanochannel creates the Leidenfrost layer. Liquid slips on vapor to decrease pressure drop in nanopores, which is similar to a droplet rolling on a super-hydrophobic wall. This phenomenon is newly recognized as the lotus-leaf-effect in nanoscale [35]. Here, the symmetry rule for homogeneous nucleation and Leidenfrost is emphasized. Both patterns are insensitive to small disturbance of the system. The symmetry geometry and boundary conditions result in symmetry parameter distribution.

4.3. Symmetry breaking of heterogeneous nucleation

Practically, due to random roughness distribution, the exact locations of bubble nucleation sites on a wall keep unknown, resulting in chaotic and bifurcation boiling [36]. Even though extensive studies have been performed for heterogeneous boiling, fundamental studies on random, chaotic and bifurcation for nanoscale boiling are seldomly reported in literature. Here, the studied problem has an exact symmetry geometry and boundary conditions. The effect of random nanobubble nucleation on asymmetric fluid densities is examined to yield the symmetry breaking. Figs. 7–10 are consecutively arranged, sharing same initial fluid density of $0.7\rho_{sat}$ and contact angle of 91.3^{o}. Figs. 7–8 are simulated using the timestep of 0.001τ and 0.0015τ, respectively, showing the effect of different timesteps on nanoscale boiling. Alternatively, Figs. 9–10 examined the effect of initial atoms distribution on nanoscale boiling, in which Fig. 9 set three coarser fluid layers near top wall and three denser fluid layers near bottom wall, while Fig. 10 set three denser fluid layers near top wall and three coarser fluid layers near bottom wall.

Even for symmetry geometry, only one wall triggers the embryo

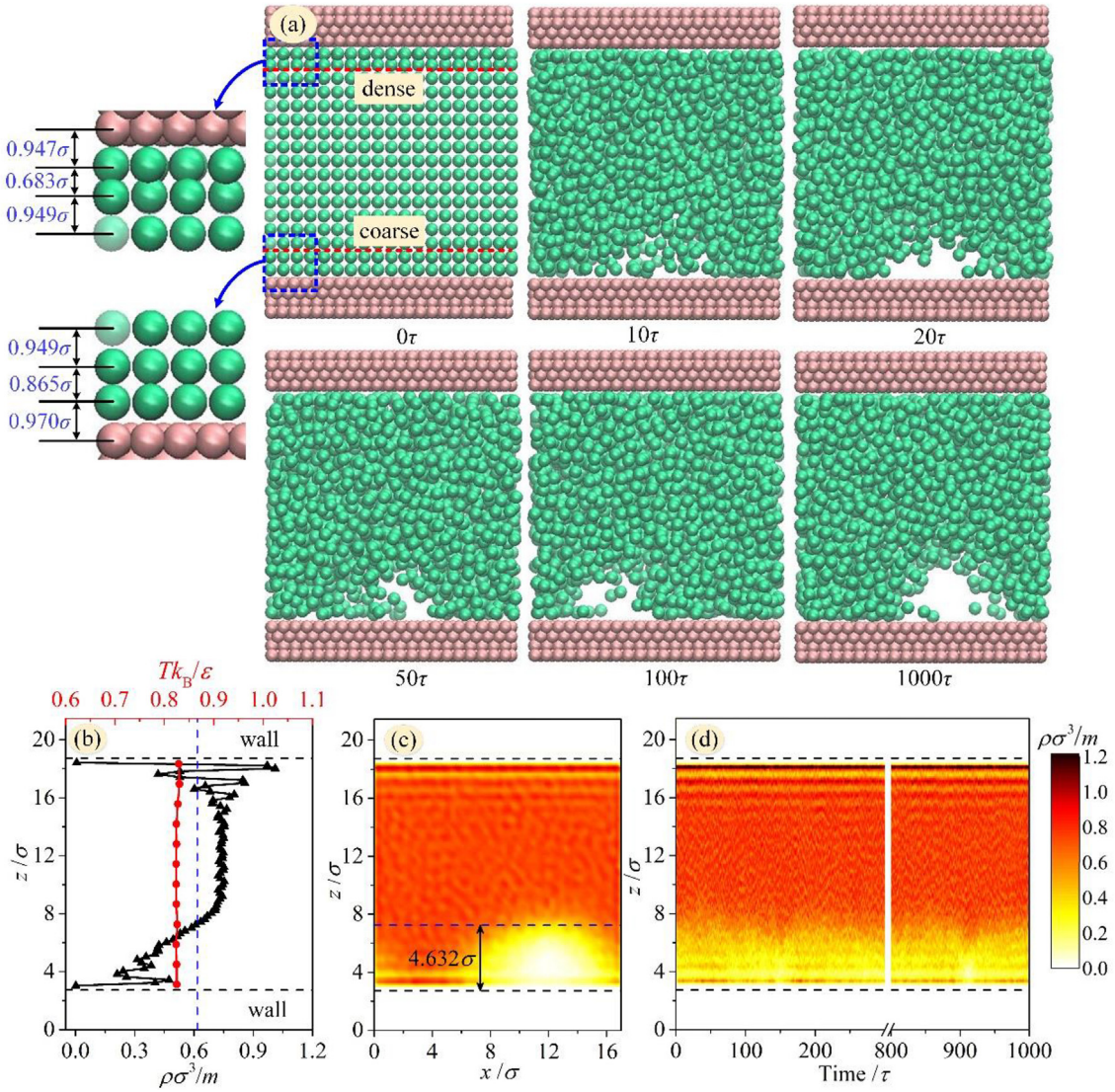

Fig. 10. Heterogeneous bubble nucleation with $\theta = 91.3°$, $\alpha = 0.14$, $\beta = 0.5$, $\rho/\rho_{sat} = 0.7$ and denser liquid atoms population near top wall (a: bubble nucleation and growth on bottom wall, b: density and temperature distributions in channel height direction, c: steady bubble over the *xz* plane, d: density evolution versus time).

nucleation, but it is impossible to trigger nucleation on both walls. For example, nucleation occurs on top wall for the timestep of 0.001τ, but on bottom wall for the timestep of 0.0015τ (see Figs. 7–8). Any numerical simulation should have numerical error, resulting in earlier formation of a bubble embryo on a specific wall, while the formation of a bubble embryo on the opposite wall is completely suppressed. Figs. 9–10 demonstrate that bubble nucleation always takes place on the wall having an initial coarser fluid atoms distribution. Random nucleation on either one of the two walls results in asymmetric fluid densities, and the bubble side has much smaller fluid densities than elsewhere beyond the bubble, see subfigure b in Figs. 7–10.

Symmetry breaking is a well-known phenomenon in physics, chemistry, biology and fluid mechanics [37]. Symmetry breaking occurs when the symmetry of the system stable state is lower than the symmetry of the interaction potentials of the system [38]. As examples of breaking the continuous translational symmetry, one can mention the freezing transition in the absence of an external potential [39], and the nucleation of bumps and bridges in capillary condensation in pores [40]. The theoretical description of symmetry breaking in fluids is based either on MD simulation and Monte Carlo simulation or on the density functional theory [41,42]. To demonstrate the asymmetric feature for nanoscale boiling, Fig. 11 illustrates the location of the center of mass (COM) and the offset distance:

$$z_{COM} = \frac{\sum_{i=1}^{N} m z_i}{mN} = \frac{\sum_{i=1}^{N} z_i}{N} \tag{9}$$

where N is the total number of fluid atoms, z_i is the coordinate in channel height direction for fluid atom i, and m is the mass of a fluid atom. The offset distance is defined as the COM location deviated from the symmetry plane at $z = z_{cen}$:

$$z_{\text{offset distance}} = z_{COM} - z_{cen} \tag{10}$$

here, $z_{cen} = 10.73\sigma$ is located in the half channel height.

Fig. 11a shows that the bottom wall nucleation elevates the COM location, corresponding to Figs. 8 and 10. The top wall nucleation lowers the COM location, corresponding to Figs. 7 and 9. Fig. 11a behaves asymmetric fluid densities for heterogeneous nucleation. The homogeneous and Leidenfrost regimes display symmetric distributions of fluid atoms, but the heterogeneous regime displays $\sim 0.6\sigma$ deviation from z_{cen} of the symmetry plane (see Fig. 11b).

The random behavior and symmetry breaking for heterogeneous nucleation are successfully demonstrated by the numerical test. The task is done by using either the different timesteps, or the different initial distribution of fluid atoms. Both methods are equivalent to

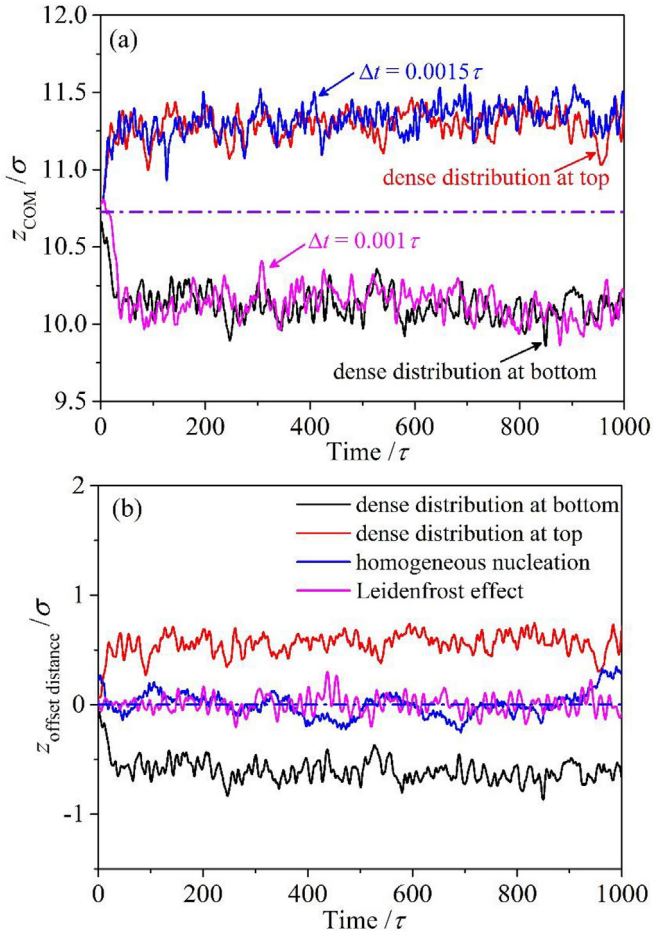

Fig. 11. The locations of the center of mass COM and their deviation from the channel centerline versus time.

introduce a very small disturbance to the system. Definitely, different timesteps result in different numerical errors, simulating different magnitudes of disturbance. Even though the wall to trigger the bubble nucleation is not fixed, the simulation results are reliable. For a practical boiling device, the random wall roughness distribution, any impurity in the fluid, or a small system shaking may trigger the heterogeneous nucleation on somewhere. This is the reason why we do not know where is the location for the first bubble nucleation site. The present study enhances the understanding of the random behavior and symmetry breaking for boiling.

4.4. Connection between wall wettability, boiling regimes and symmetry breaking

A connection between wall wettability, boiling regime and symmetry breaking is made. As shown in Fig. 12a, to form a bubble with a bubble radius r_c, the change in availability is [3].

$$\Delta\psi = \gamma_{lv}A_{lv} + (\gamma_{sv} - \gamma_{ls})A_{sv} + (P_l - P_v)V_v + \rho_v V_v(\mu_v - \mu_l) \tag{11}$$

where γ is the surface tension, μ is the chemical potential, the subscripts s, l and v represent solid, liquid and vapor, respectively. The interfacial areas are

$$A_{lv} = 2\pi r_c^2(1 + \cos\theta),\ A_{sv} = 2\pi r_c^2(1 - \cos^2\theta) \tag{12}$$

The bubble volume V_v is

$$V_v = \frac{\pi r_c^3}{3}(2 + 3\cos\theta - \cos^3\theta) \tag{13}$$

Assuming the Young-Laplace equation for pressure difference across bubble interface, the above deduction yields the change in availability during heterogeneous nucleation as

$$\Delta\psi_c = \frac{4\pi r_c^2\gamma_{lv}}{3}F(\theta) \tag{14}$$

where $F(\theta)$ is called the Fletcher factor:

$$F(\theta) = \frac{2 + 3\cos\theta - \cos^3\theta}{4} \tag{15}$$

Using the relationship between θ and β in Fig. 2c, one obtains the curve of $F(\theta)\sim\beta$ in Fig. 12b. The logic $\beta\uparrow \rightarrow \theta\downarrow \rightarrow F(\theta)\uparrow \rightarrow \Delta\psi_c\uparrow$ explains the nucleation behavior. The increase of β raises the difficulty to nucleate a bubble on the wall. At sufficiently small β such as $\beta < 0.3$, super-hydrophobic wall triggers Leidenfrost layer on the wall. At sufficiently large β such as $\beta > 0.7$, the high surface energy prevents super-hydrophilic wall from forming bubble embryo to yield homogeneous nucleation. For β values in the range of 0.3–0.7, one of the two walls triggers heterogeneous nucleation, resulting in symmetry breaking. Two critical β values dominate the transition between different regimes. The value $\beta = 0.3$ switches Leidenfrost regime to heterogeneous nucleation, and $\beta = 0.7$ switches heterogeneous nucleation to homogeneous nucleation. This conclusion is valid for the present problem. The critical values maybe changed for different boiling systems, but the general trend for the transition between different boiling regimes keeps same as shown in Fig. 12.

In this paper, homogeneous nucleation is observed with $\theta < 37°$ (see Figs. 3 and 12). The well wetting surface thoroughly suppresses heterogeneous nucleation, satisfying the minimum Gibbs free energy principle. We note that this conclusion is drawn under conditions of ideal smooth surface without wall superheating. For macroscale boiling, well wetting surface introduces the difficulty to nucleate bubbles on the wall. However, micron sized cavities and apparent wall superheating can promote bubble nucleation on the wall.

4.5. Comments on nanoscale boiling and macroscale boiling

Here, we deal with the effect of surface wettabilities on nanoscale boiling. The findings enhance the understanding of boiling in nanoscale and macroscale. First, when a fluid approaches the saturation liquid density in metastable regime, vapor voids cannot be triggered to behave uniform fluid structure. This is a distinct feature in nanoscale, but it is impossible to occur in macroscale. Second, the Leidenfrost phenomenon widely occurs in practical facilities. Usually, the vapor layer is generated by ultra-wall-heating. In this paper, the wall-attached-Leidenfrost layer in nanochannel is caused by low surface energy, not by high wall temperature. This finding is useful to reduce pressure drops for fluid transport in nanochannels.

Homogeneous nucleation needs very strict conditions such as perfect smooth wall surface and clean liquid without any impurity. Thus, homogeneous nucleation is seldomly observed in experiments. However, when these strict conditions are satisfied, the present study shows that the homogeneous nucleation indeed takes place. The nucleation location is in the fluid volume center to display symmetry behavior. Finally, it is known that heterogeneous nucleation behaves random characteristic, which is seldomly simulated in numerical works. The numerical simulation uses the deterministic method. For example, a bubble embryo is assumed in a specific location to initiate the simulation using the volume-of-fluid (VOF) interface tracking method. Here, the random boiling phenomenon is successfully simulated by varying timesteps, or the disturbance of the initial arrangement of fluid atoms. Both methods are equivalent to introduce disturbance to the system. The findings of random boiling and symmetry breaking in nanoscale explain why it is difficult to observe the first bubble embryo in macroscale boiling. Considering a boiling flow in a large size channel, because it is impossible to capture identical vapor contents over the channel cross-section at a specific time, the phase distribution cannot

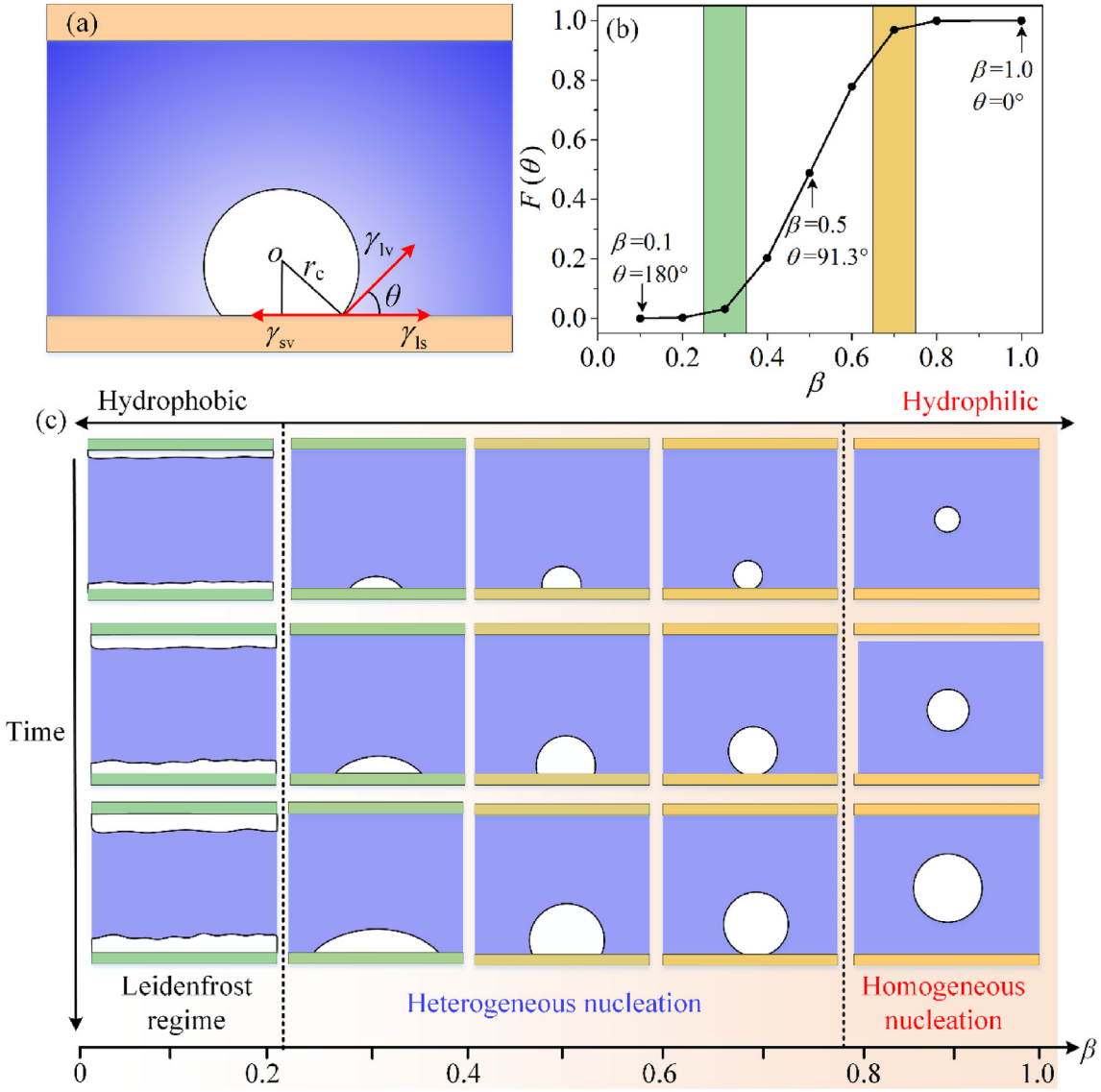

Fig. 12. Effect of wall surface wettabilities on the transition between different boiling regimes (a: geometric parameters of a bubble on a wall, b: $F(\theta)$ dependent on β, c: three boiling regimes dependent on β).

be symmetry.

5. Conclusions

Following conclusions are drawn:

- A complete boiling regime map is presented to include a non-bubble-nucleation regime for $\rho > 0.8\rho_{sat}$ and three regimes for $\rho \leq 0.8\rho_{sat}$. The regimes of Leidenfrost, heterogeneous and homogeneous occur consecutively with the increase of surface wettings from super-hydrophobicity to super-hydrophilicity.
- Non-bubble-nucleation is explained by the fact that assuming a growing bubble embryo, the increased repulsive force pulls extra atoms in liquid back to bubble, making the bubble embryo collapse. This regime is independent on wall wettabilities.
- Leidenfrost layers cover both super-hydrophobic walls, presenting a new clue to reduce pressure drops in nanopores. Both Leidenfrost and homogeneous regimes generate symmetric fluid densities.
- For heterogeneous nucleation, a bubble embryo forms on one of the two walls. A small disturbance may change the wall to nucleate a bubble embryo. The system has asymmetric fluid densities to cause symmetry breaking.
- Using surface energy analysis, the connection between surface wettability, boiling regime and symmetry breaking is made.

Acknowledgement

This work is supported by the Natural Science Foundation of China with the contract number of 51436004 and 51821004.

Appendix A. Supplementary data

Supplementary data to this article can be found online at https://doi.org/10.1016/j.ijthermalsci.2019.106033.

Nomenclature

a	footprint radius (m)
A	interfacial area (m^2)
f	exiting force (N)
F	force for pair atoms interaction (N)
$F(\theta)$	Fletcher factor

h	droplet height (m)
H	thickness of liquid film (m)
k_B	Boltzmann constant (J/K)
L_i	size parameter of system along i ($=x$, y, z) direction (m)
m	atom mass (kg)
N	number of atoms
p_i	momentum of ith solid atom (kg·m/s)
P	pressure (Pa)
r	distance between two atoms (m)
r_c	critical radius of the bubble (m)
r_d	radius of the droplet (m)
t	time (s)
T	temperature (K)
u	mean velocity (m/s)
v	laboratory velocity (m/s)
V	bubble volume (m^3)
x	x direction (m)
y	y direction (m)
z	z direction (m)

Greek symbols

α	potential energy factor indicating the strength of hydrophilic interaction
β	potential energy factor indicating the attraction for hydrophobic interaction
γ	surface tension (N/m)
δ	number of degrees of freedom
Δt	time step (s)
σ	length scale for pair potential interaction (m)
σ_G	standard deviation
ε	energy scale for pair potential interaction (J)
θ	contact angle (o)
μ	chemical potential (J)
ξ	damping constant (s^{-1})
ρ	density (kg/m^3)
τ	time scale (s)
φ	potential energy (J)
ψ	availability (J)

Subscripts

B	Boltzmann
c	critical state
cen	center
d	droplet
G	Gaussian distribution
l	liquid
s	solid
sat	saturation
v	vapor

Superscripts

het	heterogeneous nucleation
hom	homogeneous nucleation

Acronyms

fcc	face-centered-cubic structure
COM	center of mass

References

[1] J. Kim, Review of nucleate pool boiling bubble heat transfer mechanisms, Int. J. Multiph. Flow 35 (2009) 1067–1076.

[2] C.H. Wang, V.K. Dhir, Effect of surface wettability on active nucleation site density during pool boiling of water on a vertical surface, J. Heat Transf. 115 (1993) 659–669.

[3] V.P. Carey, Liquid-Vapor Phase-Change Phenomena, Hemisphere, Washington, 1992.

[4] J.C. Wei, X.R. Zhang, F. Song, Deformation of surface nanobubbles induced by substrate hydrophobicity, Langmuir 32 (2016) 13003–13008.

[5] X.H. She, T.A. Shedd, B. Lindeman, Y.G. Yin, X.S. Zhang, Bubble formation on solid surface with a cavity based on molecular dynamics simulation, Int. J. Heat Mass Transf. 95 (2016) 278–287.

[6] J.H. Weijs, J.H. Snoeijer, D. Lohse, Formation of surface nanobubbles and the universality of their contact angles: a molecular dynamics approach, Phys. Rev. Lett. 108 (2012) 104501.

[7] G. Nagayama, T. Tsuruta, P. Cheng, Molecular dynamics simulation on bubble formation in a nanochannel, Int. J. Heat Mass Transf. 49 (2006) 4437–4443.

[8] T. Yamamoto, M. Matsumoto, Initial stage of nucleate boiling: molecular dynamics investigation, J. Therm. Sci. Technol. (Tokyo, Jpn.) 7 (2012) 334–349.

[9] Y.J. Chen, J.F. Li, B. Yu, D.L. Sun, Y. Zou, D.X. Han, Nanoscale study of bubble nucleation on a cavity substrate using molecular dynamics simulation, Langmuir 34 (2018) 14234–14248.

[10] W.R. Wang, S.H. Huang, X.S. Luo, MD simulation on nano-scale heat transfer mechanism of sub-cooled boiling on nano-structured surface, Int. J. Heat Mass Transf. 100 (2016) 276–286.

[11] B.R. Novak, E.J. Maginn, M.J. McCready, An atomistic simulation study of the role of asperities and indentations on heterogeneous bubble nucleation, J. Heat Transf. 130 (2008) 042411.

[12] B.R. Novak, E.J. Maginn, M.J. McCready, Comparison of heterogeneous and homogeneous bubble nucleation using molecular simulations, Phys. Rev. B 75 (2007) 085413.

[13] V.P. Carey, A.P. Wemhoff, Thermodynamic analysis of near-wall effects on phase stability and homogeneous nucleation during rapid surface heating, Int. J. Heat Mass Transf. 48 (2005) 5431–5445.

[14] A. Hens, R. Agarwal, G. Biswas, Nanoscale study of boiling and evaporation in a liquid Ar film on a Pt heater using molecular dynamics simulation, Int. J. Heat Mass Transf. 71 (2014) 303–312.

[15] Y.H. Wang, S.Y. Wang, G. Lu, X.D. Wang, Explosive boiling of nano-liquid argon films on high temperature platinum walls: effects of surface wettability and film thickness, Int. J. Therm. Sci. 132 (2018) 610–617.

[16] T. Fu, Y. Mao, Y. Tang, Y.W. Zhang, Y. Wei, Effect of nanostructure on rapid boiling of water on a hot copper plate: a molecular dynamics study, Heat Mass Transf. 52 (2016) 1469–1478.

[17] S.M. Shavik, M.N. Hasan, A.K.M.M. Morshed, Molecular dynamics study on explosive boiling of thin liquid argon film on nanostructured surface under different wetting conditions, J. Electron. Packag. 138 (2016) 010904.

[18] W. Wang, H. Zhang, C. Tian, X. Meng, Numerical experiments on evaporation and explosive boiling of ultra-thin liquid argon film on aluminum nanostructure substrate, Nanoscale Res. Lett. 10 (2015) 158.

[19] P.A.E. Schoen, D. Poulikakos, S. Arcidiacono, Phase change of a confined subcooled simple liquid in a nanoscale cavity, Phys. Rev. E 71 (2005) 041602.

[20] S. Gong, P. Cheng, X.J. Quan, Two-dimensional mesoscale simulations of saturated pool boiling from rough surfaces. Part I: bubble nucleation in a single cavity at low superheats, Int. J. Heat Mass Transf. 100 (2016) 927–937.

[21] S. Gong, P. Cheng, Lattice Boltzmann simulations for surface wettability effects in saturated pool boiling heat transfer, Int. J. Heat Mass Transf. 85 (2015) 635–646.

[22] H.J. Jo, H.S. Ahn, S.H. Kang, M.H. Kim, A study of nucleate boiling heat transfer on hydrophilic, hydrophobic and heterogeneous wetting surfaces, Int. J. Heat Mass Transf. 54 (2011) 5643–5652.

[23] D.J. Lee, Y.S. Song, Anomalous water drop bouncing on a nanotextured surface by the Leidenfrost levitation, Appl. Phys. Lett. 108 (2016) 201604.

[24] G. Dupeux, P. Bourrianne, Q. Magdelaine, C. Clanet, D. Quéré, Propulsion on a superhydrophobic ratchet, Sci. Rep. 4 (2014) 05280.

[25] I. Malavasi, B. Bourdon, P. Di Marco, J. de Coninck, M. Marengo, Appearance of a low superheat "quasi-Leidenfrost" regime for boiling on superhydrophobic surfaces, Int. Commun. Heat Mass Transf. 63 (2015) 1–7.

[26] H.Y. Hsu, M.C. Lin, B. Popovic, C.R. Lin, N.A. Patankar, A numerical investigation of the effect of surface wettability on the boiling curve, PLoS One 12 (2017) e0187175.

[27] L.S. Zhong, Z.G. Guo, Effect of surface topography and wettability on the Leidenfrost effect, Nanoscale 9 (2017) 6219–6236.

[28] P. Yi, D. Poulikakos, J. Walther, G. Yadigaroglu, Molecular dynamics simulation of vaporization of an ultra-thin liquid argon layer on a surface, Int. J. Heat Mass Transf. 45 (2002) 2087–2100.

[29] J. Delhommelle, P. Millié, Inadequacy of the Lorentz-Berthelot combining rules for accurate predictions of equilibrium properties by molecular simulation, Mol. Phys. 99 (2001) 619–625.

[30] S. Plimpton, Fast parallel algorithms for short-range molecular dynamics, J. Comput. Phys. 117 (1993) 1–19.

[31] T. Kinjo, M. Matsumoto, Cavitation processes and negative pressure, Fluid Phase Equilib. 144 (1998) 343–350.

[32] J.J. Nicolas, K.E. Gubbins, W.B. Streett, D.J. Tildesley, Equation of state for the Lennard-Jones fluid, Mol. Phys. 37 (1979) 1429–1454.

[33] V.G. Baidakov, S.P. Protsenko, Z.R. Kozlova, Thermal and caloric equations of state for stable and metastable Lennard-Jones fluids: I. Molecular-dynamics simulations, Fluid Phase Equilib. 263 (2008) 55–63.

[34] J. Xie, J.L. Xu, W. Shang, K. Zhang, Mode selection between sliding and rolling for droplet on inclined surface: effect of surface wettability, Int. J. Heat Mass Transf. 122 (2018) 45–48.

[35] Z.Q. Yuan, H. Chen, J.D. Zhang, Facile method to prepare lotus-leaf-like superhydrophobic poly (vinyl chloride) film, Appl. Surf. Sci. 254 (2008) 1593–1598.

[36] L.H. Chai, M. Shoji, Thermodynamics bifurcations of boiling structure, Int. J. Heat Mass Transf. 45 (2002) 4675–4682.

[37] E. Ruckenstein, G.O. Berim, Symmetry breaking in confined fluids, Adv. Colloid Interface Sci. 154 (2010) 56–76.
[38] C. Yannouleas, U. Landman, Symmetry breaking and quantum correlations in finite systems: studies of quantum dots and ultracold Bose gases and related nuclear and chemical methods, Rep. Prog. Phys. 70 (2007) 2067–2148.
[39] Y. Rosenfeld, Close-packed configurations, 'symmetry breaking', and the freezing transition in density functional theory, J. Phys. Condens. Matter 8 (1996) L795–L801.
[40] A.V. Neimark, P.I. Ravikovitch, A. Vishnyakov, Bridging scales from molecular simulations to classical thermodynamics: density functional theory of capillary condensation in nanopores, J. Phys. Condens. Matter 15 (2003) 347–365.
[41] G. Germano, F. Schmid, Nematic-isotropic interfaces under shear: a molecular-dynamics simulation, J. Chem. Phys. 123 (2005) 214703.
[42] G.O. Berim, E. Ruckenstein, Two-dimensional symmetry breaking of fluid density distribution in closed nanoslits, J. Chem. Phys. 128 (2008) 024704.